Chemical Science

ROYAL SOCIETY OF CHEMISTRY

EDGE ARTICLE

View Article Online
View Journal | View Issue

Check for updates

Cite this: *Chem. Sci.*, 2025, **16**, 13514

All publication charges for this article have been paid for by the Royal Society of Chemistry

Insight into Ni active site coordination in nickel–manganese spinels for methanol electrooxidation catalysis†

Ruiying Guo,[a] Chunru Liu,[a] Yun Yang, *[b] Shuli Wang[a] and Ligang Feng *[a]

As non-precious catalysts, Ni-based catalysts play a significant role in methanol oxidation for energy conversion technologies. At the same time, the effect of the complicated chemical environment on catalytic efficiency remains unclear. Here, the coordination environment of Ni active sites in spinel nickel–manganese ($NiMn_2O_4$ and $MnNi_2O_4$) is investigated as a platform to elucidate the correlation with catalytic performance in methanol electro-oxidation. The occupation of Ni^{2+} ions in these structures modulates the intrinsic activity of Ni active sites in NiMn spinels, resulting in different catalytic mechanisms and intrinsic active site efficiency, although they have similar morphology and structure. The high-symmetry NiO_6 octahedral structure in inverse spinel $MnNi_2O_4$ exhibits superior catalytic performance and stability compared to the NiO_4 tetrahedral structure in normal $NiMn_2O_4$ spinel. Specifically, at 1.50 V *vs.* RHE, the $MnNi_2O_4$ inverse spinel delivers mass activity and specific activity for methanol oxidation that are 1.9 and 3.5 times those of the normal $NiMn_2O_4$ spinel, respectively. Furthermore, it also maintains a stable current density of 33.5 mA cm^{-2} at 1.56 V *vs.* RHE for 25 hours. Theoretical calculations reveal that Ni sites in $MnNi_2O_4$ exhibit a significantly lower activation energy barrier and enhanced CO anti-poisoning capability compared to those in $NiMn_2O_4$. The Ni site-dependent coordination environment in spinel structures provides useful insights into catalyst development and the methanol oxidation mechanism.

Received 21st April 2025
Accepted 23rd June 2025

DOI: 10.1039/d5sc02883c

rsc.li/chemical-science

Open Access Article. Published on 26 June 2025. Downloaded on 2/14/2026 4:46:11 AM.
This article is licensed under a Creative Commons Attribution-NonCommercial 3.0 Unported Licence.

Introduction

Electrocatalytic water splitting holds a pivotal position in sustainable hydrogen generation.[1–3] Nevertheless, the oxygen evolution reaction (OER), a multielectron transfer process, suffers from sluggish kinetics and high energy demands.[4–6] Recent attention has shifted toward the anodic oxidation of small organic molecules to facilitate hydrogen production, with a particular focus on the methanol oxidation reaction (MOR).[7–9] This is mainly due to its low overpotential (0.016 V) and high energy efficiency (~60%), making it a promising alternative.[10,11]

To fulfil efficient MOR catalysis, attention is directed to non-noble metal catalysts since platinum group metals (PGMs) are restricted by high cost and susceptibility to CO poisoning.[12,13] Ni-based materials, in particular, show great promise as MOR catalysts, including Ni-hydroxides, perovskites, and layered double hydroxides.[14,15] During the methanol reaction, the active high-valent NiOOH intermediate is inevitably formed from the pre-catalyst and serves as a chemical oxidant that converts methanol to carbon dioxide while being reduced to $Ni(OH)_2$.[16] Tuning the coordination environment of Ni sites has proven to be an effective strategy to improve catalytic efficiency, as it not only determines the electronic structures of Ni active sites but also governs the reaction mechanisms.[17,18] For example, Mo-doped $Ni(OH)_2$ with ultralow Ni–Ni coordination enhanced the interaction between OH^- and CH_3OH at the Ni active center, thereby promoting both the kinetics and durability of methanol electrocatalysis.[19] A stable NiSnPH perovskite hydroxide, obtained *via* selective Sn leaching, optimized the local coordination environment of NiOOH active sites, resulting in enhanced selectivity for methanol oxidation to formate.[20] Among Ni-based catalysts, particularly NiMn-based spinel oxides were effective for the MOR due to their stable crystal structures, controllable compositions, and polymetallic synergies.[21,22] For instance, multi-walled carbon nanotube (MWCNT)- or reduced graphene oxide (rGO)-supported $MnNi_2O_4$ showed favourable MOR activity benefiting from the binary transition metal oxides' synergism.[23,24] While Ni sites in the spinel structure serve as active sites to trigger methanol oxidation, their precise catalytic mechanism remains unclear. Actually, Ni sites would be an ideal platform to probe intrinsic activity and reveal the effect of the Ni coordination environment in the spinels on catalytic performance. For example, the Ni active sites in spinel nickel–

[a]*School of Chemistry and Chemical Engineering, Yangzhou University, Yangzhou 225002, P. R. China. E-mail: ligang.feng@yzu.edu.cn; fenglg11@gmail.com*

[b]*Nanomaterials and Chemistry Key Laboratory, Wenzhou University, Wenzhou, P. R. China. E-mail: bachier@163.com*

† Electronic supplementary information (ESI) available. See DOI: https://doi.org/10.1039/d5sc02883c

© 2025 The Author(s). Published by the Royal Society of Chemistry

Open Access Article. Published on 26 June 2025. Downloaded on 2/14/2026 4:46:11 AM. This article is licensed under a Creative Commons Attribution-NonCommercial 3.0 Unported Licence.

manganese (NiO_4 tetrahedral structure for $NiMn_2O_4$ and NiO_6 octahedral structure for $MnNi_2O_4$) could be used to elucidate the connection between Ni site coordination and catalytic performance. However, to the best of our knowledge, no relevant reports have specifically addressed this concern.

In this study, we take NiMn-based spinel catalysts ($NiMn_2O_4$ and $MnNi_2O_4$) as a platform to explore the correlation between the Ni coordination environment in various spinel structures and catalytic performance for the MOR. $MnNi_2O_4$ spinel, with Ni sites in an octahedral configuration, exhibits significantly enhanced performance compared to the normal $NiMn_2O_4$ spinel. Specifically, at 1.50 V *vs.* RHE, the $MnNi_2O_4$ inverse spinel delivers mass activity and specific activity that are 1.9 and 3.5 times those of the normal $NiMn_2O_4$ spinel, respectively. Furthermore, it also maintains a stable current density of 33.5 mA cm^{-2} at 1.56 V *vs.* RHE for 25 hours. This enhancement stems from the presence of highly active Ni sites in the NiO_6 octahedral coordination environment of $MnNi_2O_4$, contributing to excellent intrinsic catalytic efficiency. Theoretical analysis demonstrates a lower activation threshold and superior CO anti-poisoning ability of Ni sites in $MnNi_2O_4$ compared to $NiMn_2O_4$. The Ni site-dependent coordination environment in spinel structures provides new insights into catalyst development and the methanol oxidation mechanism.

Experimental

Materials fabrication

In the synthesis of $MnNi_2O_4$ spinel (Fig. S1†), 1.49 g (5.98 mmol) of $Ni(CH_3COO)_2 \cdot 4H_2O$, 1.47 g (5.95 mmol) of $Mn(CH_3COO)_2 \cdot 4H_2O$, and 80 mL of ultrapure water were added into a 100 mL beaker under magnetic stirring. The pH of the solution was adjusted to 10 by the dropwise addition of 5 mol per L NaOH solution, followed by stirring at room temperature for about 15 minutes. Then, the mixture was transferred to a 150 mL Teflon-lined autoclave and heated at 150 °C for 12 hours. After natural cooling to room temperature, the synthesized product was collected by centrifuging, washed several times with ultrapure water and anhydrous ethanol, and then dried under vacuum at 60 °C for 8 hours. Finally, the dried powder was annealed in air at 800 °C for 2 hours and cooled to room temperature to obtain $MnNi_2O_4$ spinel. The $NiMn_2O_4$ spinel was synthesized by a similar method with different molar ratios of nickel acetate tetrahydrate and manganese acetate tetrahydrate. The NiO and Mn_2O_3 samples were fabricated for performance comparisons (Table S1†).

Materials characterization

The crystal structure was probed using powder X-ray diffraction (XRD) patterns which were obtained on a Bruker D8 Advance with a Cu K_α radiation source ($\lambda = 1.5405$ Å) under operating conditions of 40 kV and 40 mA, with a scan rate of 5° min^{-1}. The morphology of the $NiMn_2O_4$ and $MnNi_2O_4$ spinels was analyzed by using a scanning electron microscope (SEM, Hitachi, S-4800 II, Japan) and transmission electron microscopy (TEM) and high-resolution TEM (HRTEM) measurements (TECNAI G2 operating at 300 kV). The energy-dispersive X-ray detector spectrum (EDS) was obtained on a TECNAI G2 transmission electron microscope equipped with an EDXA detector. The chemical state of the surface was probed using X-ray photoelectron spectroscopy (XPS) with a K_α radiation source.

All the electrochemical tests were done using a Bio-Logic VSP electrochemical workstation (Bio-Logic Co., France) in a conventional three-electrode system. The working electrode was obtained by dropping catalyst ink over a glassy carbon electrode (3.0 mm diameter, 0.07 cm^2). The catalyst ink was prepared by ultrasonically mixing 4.5 mg of catalyst, 0.5 mg of carbon black, 950 μL of ethanol, and 50 μL of Nafion solution. 10 μL of the catalyst ink was coated over the electrode and dried naturally before electrochemical testing. A graphite rod and saturated calomel electrode (SCE, Hg/Hg_2Cl_2) were used as the counter and reference electrodes, respectively. All the potentials were converted to the reversible hydrogen electrode (RHE).

Cyclic voltammetry (CV) tests were conducted in 1 M KOH solution or 1 M KOH + 1 M CH_3OH solution with a voltage range of 1.06–1.66 V *vs.* RHE at 50 mV s^{-1}. The electrochemical impedance spectra (EIS) were recorded at frequencies ranging from 1000 kHz to 10 mHz with an amplitude of 5 mV in the above electrode system. The electrochemical surface area (ECSA) was calculated using the redox peak of Ni^{3+}/Ni^{2+} in the backward scan of CV curves in the KOH solution. The charge during the cathodic reduction peak of Ni^{3+}/Ni^{2+} was calculated using a factor of 0.257 mC cm^{-2} (0.257 mC cm^{-2} is the charge required to form a monolayer of Ni^{2+}). The chronoamperometry (CA) experiment was performed at 1.56 V *vs.* RHE for 25 hours in 1 M KOH + 1 M CH_3OH solution. The materials, some formulae for the performance calculation, and the theoretical analysis can be found in the ESI.†

Results and discussion

The three-dimensional (3D) spinel structures of $NiMn_2O_4$ and $MnNi_2O_4$ are illustrated in Fig. 1a. Both crystallize in the $Fd\bar{3}m$ space group and feature a characteristic structure where metal cations (Ni and Mn) are distributed across tetrahedral and octahedral coordination sites. The coordination structure in these compounds varies slightly with oxidation states due to their mixed valency. In $NiMn_2O_4$, Ni^{2+} ions typically occupy tetrahedral (A) sites, where each metal ion is coordinated to four oxygen atoms, while Mn^{3+} ions reside in octahedral (B) sites, coordinated to six oxygen atoms. These metal cations are bridged by oxygen ions (O^{2-}). In the simplified structure, the A sublattice contains Ni^{2+} ions in tetrahedral sites (A), while the B sublattice contains Mn^{3+} ions in octahedral sites (B). $MnNi_2O_4$ adopts a similar spinel-type structure to $NiMn_2O_4$ but exhibits an inverse cation distribution because of its different stoichiometry. In this simplified structure, Ni^{2+} ions preferentially occupy octahedral (B) sites, while Mn^{4+} ions reside in tetrahedral (A) sites.

During fabrication, as Ni is added, Ni^{2+} ions progressively replace Mn^{3+} ions at octahedral positions, facilitating the formation of the inverse spinel structure. Upon transformation of $NiMn_2O_4$ into $MnNi_2O_4$, the $MnNi_2O_4$ inverse spinel phase

Open Access Article. Published on 26 June 2025. Downloaded on 2/14/2026 4:46:11 AM.
This article is licensed under a Creative Commons Attribution-NonCommercial 3.0 Unported Licence.

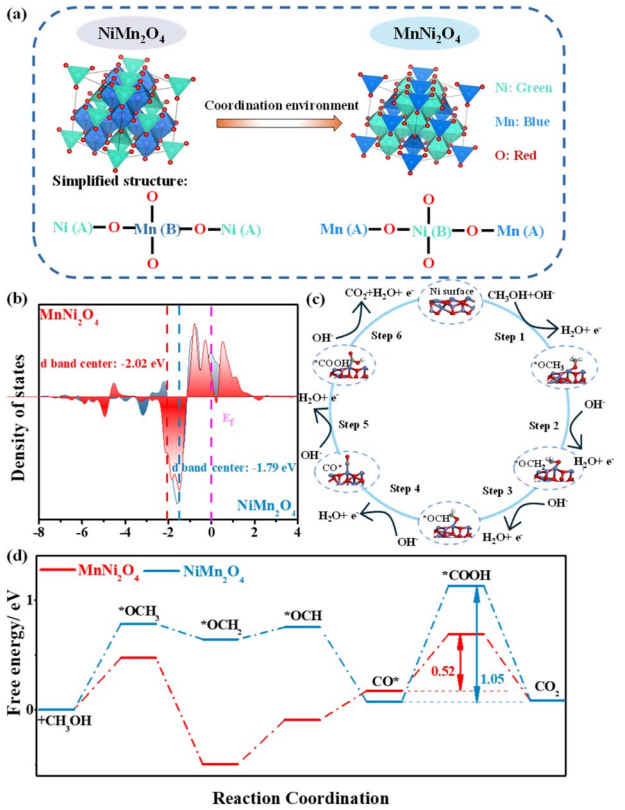

Fig. 1 (a) Structure models of $NiMn_2O_4$ and $MnNi_2O_4$ spinels: the transformation of Ni^{2+} from tetrahedral to octahedral coordination. (b) The partial density of states (PDOS) of $NiMn_2O_4$ and $MnNi_2O_4$ surfaces. (c) Diagram of the reaction process of the MOR on the $MnNi_2O_4$–Ni site. (d) The Gibbs free energy diagram for the MOR of $NiMn_2O_4$ and $MnNi_2O_4$.

with a high-coordination NiO_6 octahedral structure exhibits enhanced crystal symmetry and stabilizes the spinel structure. Moreover, the increased number of Ni^{2+} ions in octahedral geometry generates more active Ni oxidation sites. Conversely, the low-coordination NiO_4 tetrahedral structure in $NiMn_2O_4$ destabilizes the spinel structure. Thus, the occupation of Ni^{2+} ions in these structures modulates the intrinsic activity of Ni active sites in NiMn spinels.[25]

Given the superior MOR performance of $MnNi_2O_4$ to $NiMn_2O_4$ (*vide infra*), density functional theory (DFT) calculations were performed on optimized surface models of Ni and Mn sites in $MnNi_2O_4$ to evaluate the catalytic efficiency of distinct active sites (Fig. S2–S4†).[26] Both Ni^{2+} ions preferentially occupied octahedral (B) sites, forming a $Mn^{4+}[Ni_2^{2+}]O_4^{2-}$ valence structure.[27] The octahedral NiO_6 structure showed significantly higher MOR performance than the MnO_4 structure, consistent with previous studies (Fig. S5†).[28] To elucidate the influence of the Ni site coordination environment on electrocatalytic performance, we compared the Ni d-band centers of $MnNi_2O_4$ and $NiMn_2O_4$. The Ni d-band center in $MnNi_2O_4$ (−2.02 eV) was more negative than that in $NiMn_2O_4$ (−1.79 eV), moving further from the Fermi level owing to the robust synergistic effect between Ni d orbitals and O p orbitals (Fig. 1b). This shift enhances charge transfer efficiency and reduces intermediate adsorption.[29] The carbon monoxide intermediate (CO*) adsorption energy (E_{CO*}) is also a key descriptor of MOR catalytic performance. $MnNi_2O_4$ exhibited a lower E_{CO*} value (−1.13 eV) relative to $NiMn_2O_4$ (−1.24 eV), indicating enhanced CO poisoning resistance capacity (Fig. S6†). The widely accepted mechanism for the MOR catalyzed by Ni-based catalysts follows a stepwise process (Fig. 1c): Ni sites first serve as active centers for methanol adsorption, followed by a sequence of deprotonation steps leading to the formation of multiple bonded intermediates, all of which are formed at Ni sites and eventually convert to CO_2.[30] The overall MOR pathway can be described as follows: $*OCH_3 \rightarrow *OCH_2 \rightarrow *OCH \rightarrow CO* \rightarrow *COOH \rightarrow CO_2$. Gibbs free energy analysis revealed that the CO* → *COOH conversion was the rate-determining step (RDS) in the MOR pathway (Fig. 1d). The energy barrier for this step in $MnNi_2O_4$ (0.52 eV) was significantly lower than that in $NiMn_2O_4$ (1.05 eV), indicating more favorable MOR kinetics. Consequently, changes in the coordination environment of Ni active sites not only modulate MOR activation energies but also influence CO poisoning resistance.

The crystal structures of $NiMn_2O_4$ and $MnNi_2O_4$ were confirmed by powder X-ray diffraction (XRD), with both

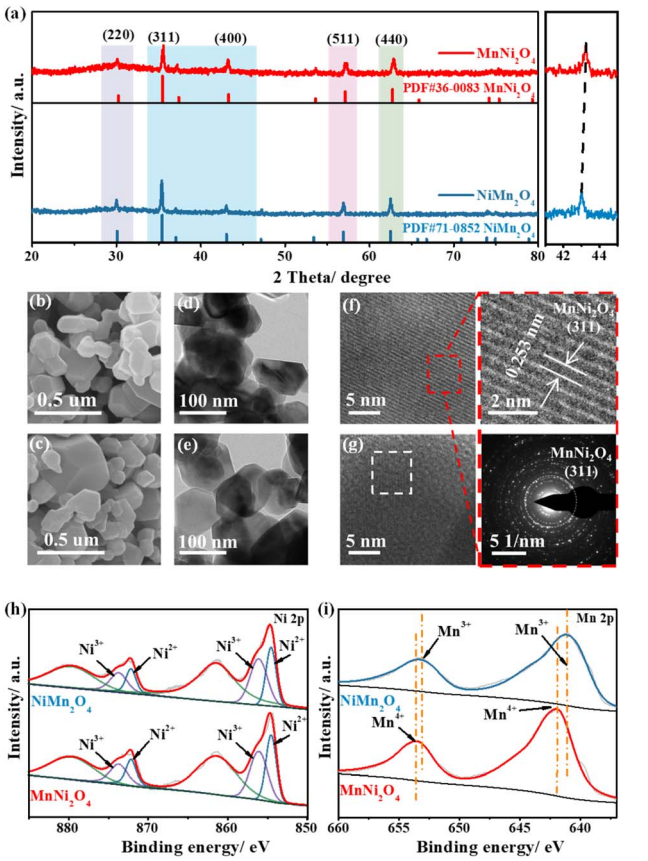

Fig. 2 (a) XRD patterns of $NiMn_2O_4$ and $MnNi_2O_4$. (b) SEM image, (d) TEM image, (f) HRTEM image and SAED pattern of $MnNi_2O_4$. (c) SEM image, (e) TEM image, and (g) HRTEM image of $NiMn_2O_4$. Ni 2p (h) and Mn 2p XPS spectra (i) of $NiMn_2O_4$ and $MnNi_2O_4$.

© 2025 The Author(s). Published by the Royal Society of Chemistry

Open Access Article. Published on 26 June 2025. Downloaded on 2/14/2026 4:46:11 AM.
This article is licensed under a Creative Commons Attribution-NonCommercial 3.0 Unported Licence.

belonging to the face-centered cubic (fcc) structure and $Fd\bar{3}m$ (227) space group (Fig. 2a). The characteristic peaks of $MnNi_2O_4$ closely resembled those of $NiMn_2O_4$, but were slightly shifted to high angles at 43.2°, 57.1°, and 62.7°, indicating that Ni^{2+} ions successfully occupied octahedral positions. Scanning electron microscopy (SEM) images revealed that both $NiMn_2O_4$ and $MnNi_2O_4$ exhibited irregular aggregated particles (Fig. 2b and c). Transmission electron microscopy (TEM) images showed a similar morphology, with irregular hexagonal planes observed for both samples (Fig. 2d and e). High-resolution TEM (HRTEM) images showed distinct lattice fringes with a *d*-spacing of 0.253 nm, assigned to the (311) planes of $MnNi_2O_4$ and $NiMn_2O_4$ spinel structures (Fig. 2f and g). Energy dispersive X-ray spectroscopy (EDS) confirmed the Ni, Mn, C, and O within the samples (Fig. S7†). The elemental mapping images showed the uniform distribution of Ni, Mn, and O elements in the $MnNi_2O_4$ spinel (Fig. S8†).

Though they have similar morphology and structure, variations in the coordination environment likely alter the chemical states of Ni sites. X-ray photoelectron spectroscopy (XPS) was thus conducted to explore the chemical states. The XPS survey spectra revealed the presence of C, O, Ni, and Mn, with the binding energy calibrated to the C–C bond reference peak at 284.8 eV (Fig. S9†). The high-resolution Ni 2p spectrum displayed two distinct peaks, corresponding to Ni $2p_{1/2}$ and Ni $2p_{3/2}$ (Fig. 2h). $MnNi_2O_4$ showed prominent double peaks of Ni^{2+} located at 854.5 and 872.1 eV, while the weak double peaks at 856.1 and 873.7 eV were attributed to Ni^{3+} (Table S2†). The Ni peak shifted from 854.8 eV in $NiMn_2O_4$ to 854.5 eV in $MnNi_2O_4$, indicating that more Ni^{2+} species occupied the octahedral sites.[31] The Ni^{3+}/Ni^{2+} intensity ratio increased from $NiMn_2O_4$ (0.89) to $MnNi_2O_4$ (1.38), which was attributed to easier surface oxidation and an increased oxidation state at the octahedral sites (Table S2†). For the Mn 2p spectrum, the deconvoluted spectrum of $MnNi_2O_4$ displayed two major peaks at 644.8 and 656.4 eV, corresponding to Mn^{4+}, whereas for $NiMn_2O_4$, the peak positions were shifted to lower energies at 642.7 and 654.3 eV, assigned to Mn^{3+} (Fig. 2i and Table S3†).[32] The high-resolution O 1s spectrum exhibited three characteristic peaks at 529.8, 531.0, and 532.4 eV, assigned to metal–oxygen bonds, adsorbed hydroxide groups, and adsorbed water molecules, respectively (Fig. S10†).

To investigate the catalytic performance in different coordination environments, electrochemical experiments were conducted on the synthesized catalysts for the MOR. CV measurements of $MnNi_2O_4$, $NiMn_2O_4$, NiO, and Mn_2O_3 electrodes in 1 M KOH with and without 1 M CH_3OH indicated that Ni-based electrodes exhibited higher MOR performance, while the Mn_2O_3 electrode showed negligible activity, suggesting that Ni sites served as the active sites for the MOR (Fig. S11†). For $MnNi_2O_4$, the oxidation peak was assigned to the Ni^{2+}/Ni^{3+} redox transition, followed by a rapid increase in the anode current density for both OER and MOR processes (Fig. 3a). The onset potential for the MOR was more negative relative to the OER, and the methanol oxidation closely coincided with the redox peak, while water oxidation occurred after the Ni^{3+} oxidation, suggesting the high energy efficiency of the MOR.[33]

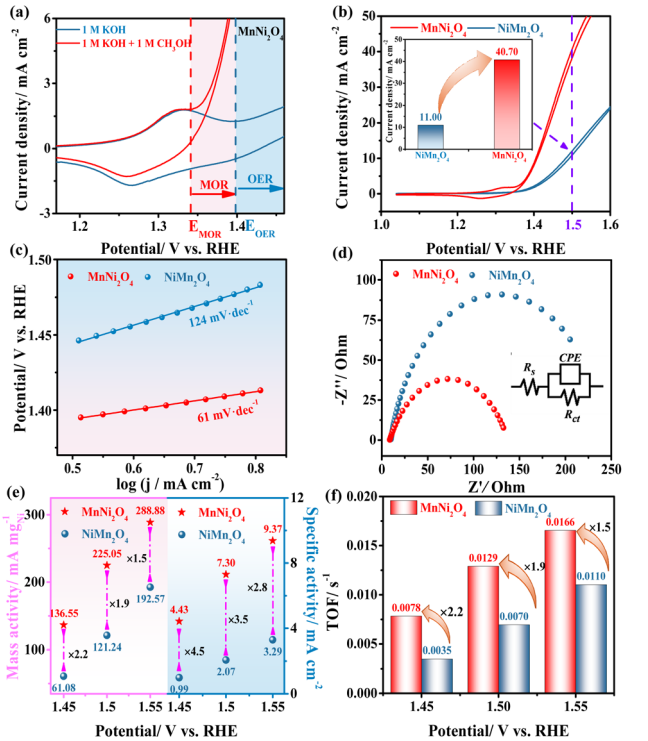

Fig. 3 (a) Cyclic voltammetry curves of $MnNi_2O_4$ measured in 1 M KOH with and without 1 M CH_3OH at 50 mV s^{-1}. (b) CV curves of $NiMn_2O_4$ and $MnNi_2O_4$ measured in 1 M KOH with 1 M CH_3OH at 50 mV s^{-1} (inset: current density at 1.50 V *vs.* RHE). (c) Tafel plots of $NiMn_2O_4$ and $MnNi_2O_4$. (d) Nyquist plots of $NiMn_2O_4$ and $MnNi_2O_4$ at 1.56 V *vs.* RHE (inset: an equivalent circuit model used for fitting the EIS data). (e) Mass activity and specific activity. (f) TOF of $NiMn_2O_4$ and $MnNi_2O_4$ at 1.45, 1.50, and 1.55 V *vs.* RHE.

By comparing the MOR performance of $MnNi_2O_4$ and $NiMn_2O_4$ electrodes, $MnNi_2O_4$ displayed a much higher forward current density of 40.7 mA cm^{-2} at 1.50 V *vs.* RHE compared to $NiMn_2O_4$ (11.0 mA cm^{-2}) (Fig. 3b). Among state-of-the-art non-precious catalysts for methanol oxidation, the $MnNi_2O_4$ spinels ranked the top in their family (Table S4†).

The MOR kinetics were evaluated by using the Tafel slope and electrochemical impedance spectroscopy (EIS). $MnNi_2O_4$ exhibited a lower Tafel slope of 61 mV dec^{-1} compared to $NiMn_2O_4$ (124 mV dec^{-1}) (Fig. 3c), indicating different catalytic mechanisms, namely, Eley–Rideal (E–R) and Langmuir–Hinshelwood (L–H) mechanisms, respectively.[34] Additionally, the E–R mechanism for the $MnNi_2O_4$ electrode supported the notion that the absorbed CO* interacted directly with OH^- from the alkaline solution and was subsequently oxidized to CO_2, which was consistent with the reaction mechanism discussed earlier. The charge transfer resistance (R_{ct}) for the $MnNi_2O_4$ electrode was 128 Ω, much lower than that of $NiMn_2O_4$ (253 Ω) (Fig. 3d and Table S5†), indicating faster reaction kinetics due to the highly active octahedrally occupied Ni^{2+} in $MnNi_2O_4$. The electrochemical stability of the as-prepared catalysts was assessed through a long-term chronoamperometric (CA) test conducted at 1.56 V *vs.* RHE for 25 hours (Fig. S12†). Initially, the current density of both $MnNi_2O_4$ and $NiMn_2O_4$ declined

Open Access Article. Published on 26 June 2025. Downloaded on 2/14/2026 4:46:11 AM. This article is licensed under a Creative Commons Attribution-NonCommercial 3.0 Unported Licence.

rapidly due to the diffusion-controlled MOR, but $MnNi_2O_4$ maintained a higher current density of 33.5 mA cm^{-2} over time than $NiMn_2O_4$, indicating good stability for the MOR. Moreover, the structure and morphology of $MnNi_2O_4$ catalysts after the stability test exhibited no evident changes, confirming their good anti-corrosion ability for long-term operation (Fig. S13†).

Since $MnNi_2O_4$ contained two Ni sites, a fair comparison of intrinsic catalytic activity was necessary. To verify the correlation between the oxidation equivalence of Ni active sites and intrinsic catalytic activity for the MOR, commonly used methods for intrinsic activity comparison, including mass activity (MA), specific activity (SA), and turnover frequency (TOF), were employed. By normalizing the current to the Ni mass amount on the electrode, $MnNi_2O_4$ exhibited enhanced electrocatalytic mass activity compared to $NiMn_2O_4$ (Fig. S14a†).[35,36] The electrochemical active surface area (ECSA) was calculated from the characteristic Ni redox peaks (Table S6†). $MnNi_2O_4$ showed a higher ECSA value of 0.39 cm^2 than $NiMn_2O_4$ (0.37 cm^2), indicating slightly greater exposure to active Ni species. More significantly, when normalizing the current to the ECSA, $MnNi_2O_4$ still showed higher specific activity than $NiMn_2O_4$ (Fig. S14b†). The typical performance comparison for both mass activity and specific activity at 1.45, 1.50, and 1.55 V *vs.* RHE is shown in Fig. 3e and Table S6.† Specifically, at 1.50 V *vs.* RHE, the mass and specific activities of $MnNi_2O_4$ were 1.9 and 3.5 times those of the $NiMn_2O_4$ electrode, respectively. Assuming that all the Ni sites were in the active phase, the TOF was calculated (Fig. S15†). At 1.45, 1.50, and 1.55 V *vs.* RHE, the $MnNi_2O_4$ electrode exhibited values of 0.0078, 0.0129, and 0.0165 s^{-1}, respectively, about 2.2, 1.9, and 1.5 times those of $NiMn_2O_4$ (Fig. 3f and Table S7†). These results conclusively showed that Ni sites in $MnNi_2O_4$ have significantly higher intrinsic activity than those of $NiMn_2O_4$.

As mentioned in the above theoretical calculation, the Mn sites are not active for the MOR, but the different Mn oxidation states would influence the performance, as they contribute to the different coordination states of Ni active sites. Additionally, the XPS analysis revealed that the high-valent Mn^{4+} in $MnNi_2O_4$ induced a stronger electronic interaction with Ni sites, promoting the formation of high-valence Ni species and further improving the MOR catalytic performance. Furthermore, it should be pointed out that due to the surface oxidation driven by high potentials, the valence state of Ni sites is increased as can be seen in the Ni redox peaks. In the current study, we revealed the effect of the coordination environment of Ni active sites in nickel–manganese spinels on methanol electrooxidation. It would be more interesting to correlate the surface chemical state changes with the catalytic ability in future studies.

Conclusions

In summary, the Ni active sites in nickel–manganese spinels were probed for methanol oxidation catalysis. Though they have similar morphology and structure, changes in the coordination environment of Ni sites influence their catalytic performance in the MOR. The inverse spinel $MnNi_2O_4$, characterized by Ni active sites in octahedral coordination, offers a high density of exposed Ni sites with superior intrinsic activity, thereby achieving exceptional catalytic performance and durability. Notably, $MnNi_2O_4$ exhibits mass and specific activities more than twice those of $NiMn_2O_4$. Theoretical calculations reveal a significantly lower activation energy barrier and enhanced CO anti-poisoning capability of Ni sites in $MnNi_2O_4$ compared to $NiMn_2O_4$. The dependence of catalytic efficiency on the coordination environment of Ni sites provides critical insights into the catalytic mechanism of the methanol oxidation reaction.

Data availability

The data supporting this article have been included as part of the ESI.†

Author contributions

Ruiying Guo: conceptualization, methodology, investigation, validation, writing the original draft. Chunru Liu: formal analysis, investigation, validation. Yun Yang: formal analysis, investigation. Shuli Wang: methodology, investigation, and formal analysis. Ligang Feng: writing-review & editing, sources, and funding.

Conflicts of interest

There are no conflicts to declare.

Acknowledgements

This work was supported by the National Natural Science Foundation of China (22272148, and 22202172).

Notes and references

1 Y. Guo, X. Zou, X. Wei, W. Bao, J. Zhang, J. Han and F. Jia, *Chin. J. Struct. Chem.*, 2024, **43**, 100206.
2 C. Liu and L. Feng, *Chin. J. Struct. Chem.*, 2023, **42**, 100136.
3 A. S. Jamadar, R. Sutar, S. Patil, R. Khandekar and J. B. Yadav, *Mater. Rep.: Energy*, 2024, **4**, 100283.
4 S. Pan, Z. Yang and F. Luo, *Chin. J. Struct. Chem.*, 2024, **43**, 100373.
5 S. Pan, Z. Ma, W. Yang, B. Dongyang, H. Yang, S. Lai, F. Dong, X. Yang and Z. Lin, *Mater. Rep.: Energy*, 2023, **3**, 100212.
6 Y. Lim, S. Surendran, W. So, S. Shanmugapriya, C. Jo, G. Janani, H. Choi, H. S. Han, H. Choi, Y.-H. Yun, T.-H. Kim, M.-J. Kim, K. Jin, J. K. Kim and U. Sim, *Mater. Chem. Front.*, 2023, **7**, 5843–5857.
7 D. Yan, C. Mebrahtu, S. Wang and R. Palkovits, *Angew. Chem., Int. Ed.*, 2023, **62**, e202214333.
8 S. Ali, P. M. Ismail, F. Wahid, A. Kumar, M. Haneef, F. Raziq, S. Ali, M. Javed, R. U. Khan, X. Wu, H. Xiao, G. Yasin, L. Qiao and H. Xu, *Fuel Process. Technol.*, 2022, **236**, 107427.

© 2025 The Author(s). Published by the Royal Society of Chemistry

Open Access Article. Published on 26 June 2025. Downloaded on 2/14/2026 4:46:11 AM.
This article is licensed under a Creative Commons Attribution-NonCommercial 3.0 Unported Licence.

9 G. Bharath, G. Karthikeyan, A. Kumar, J. Prakash, D. Venkatasubbu, A. Kumar Nadda, V. Kumar Gupta, M. Abu Haija and F. Banat, *Appl. Energy*, 2022, **318**, 119244.
10 J. Li, F. Yang and L. Feng, *Coord. Chem. Rev.*, 2025, **534**, 216603.
11 Y. Kuang, W. Qiao, S. Wang, F. Yang and L. Feng, *ACS Mater. Lett.*, 2024, **6**, 1722–1731.
12 J. Li, M. Li, F. Yang and L. Feng, *Chin. J. Chem.*, 2025, **43**, 146–154.
13 M. Li, F. Yang, J. Chang, A. Schechter and L. Feng, *Acta Phys.-Chim. Sin.*, 2023, **39**, 2301005.
14 H. Cheng, B. Dong, Q. Liu and F. Wang, *J. Am. Chem. Soc.*, 2023, **145**, 26858–26862.
15 Y. Yi, J. Li and C. Cui, *Chin. Chem. Lett.*, 2022, **33**, 1006–1010.
16 C. Liu, F. Yang, A. Schechter and L. Feng, *Adv. Sens. Energy Mater.*, 2023, **2**, 100055.
17 S. Li, R. Ma, J. Hu, Z. Li, L. Liu, X. Wang, Y. Lu, G. E. Sterbinsky, S. Liu, L. Zheng, J. Liu, D. Liu and J. Wang, *Nat. Commun.*, 2022, **13**, 2916.
18 G. Janani, S. Surendran, D. J. Moon, P. S. Ramesh, J. Y. Kim, Y. Lim, K. Veeramani, S. Mahadik, S. C. Jesudass, J. Choi, I. G. Kim, P. Jung, H. Choi, G. Kwon, K. Jin, J. k. Kim, Y. I. Park, J. Heo, K. Hong, Y. S. Kang and U. Sim, *Adv. Sustainable Syst.*, 2024, **8**, 2400059.
19 G. Fu, X. Kang, Y. Zhang, X. Yang, L. Wang, X.-Z. Fu, J. Zhang, J.-L. Luo and J. Liu, *Nano-Micro Lett.*, 2022, **14**, 200.
20 J. Shao, Y. Fang, X. Wu, M. I. Abdullah and Y. Tao, *Nano Res.*, 2024, **17**, 2388–2399.
21 H. Tian, X. Wang, W. Luo, R. Ma, X. Yu, S. Li, F. Kong, X. Cui and J. Shi, *Chem. Sci.*, 2024, **15**, 11013–11020.
22 S. Cyril Jesudass, S. Surendran, G. Janani, T.-H. Kim, Y. I. Park and U. Sim, *Appl. Surf. Sci.*, 2025, **688**, 162352.
23 S. Hosseini, M. B. Askari and H. Beitollahi, *Int. J. Hydrogen Energy*, 2023, **48**, 21240–21248.
24 M. B. Askari, P. Salarizadeh, A. Di Bartolomeo and F. Şen, *Nanotechnology*, 2021, **32**, 325707.
25 T. Zhang, Y. Liu, L. Tong, J. Yu, S. Lin, Y. Li and H. J. Fan, *ACS Nano*, 2023, **17**, 6770–6780.
26 S. Song, X. Huang, Y. Yang and L. Feng, *Chem. Commun.*, 2024, **60**, 10906–10909.
27 A. B. Devale and D. K. Kulkarni, *J. Phys. C: Solid State Phys.*, 1982, **15**, 899.
28 M. Ahmad, Q. Riaz, M. Tabassum, S. S. Shafqat, A. t. Ayesha, M. Zubair, Y. Xiong, A. Syed, H. A. Al-Shwaiman, M. A. Nadeem, X. Jia, G. Xu and M. N. Zafar, *RSC Adv.*, 2024, **14**, 28285–28297.
29 J. Li, C. Wu, Z. Wang, H. Meng, Q. Zhang, Y. Tang, A. Zou, Y. Zhang, H. Zhong, S. Xi, J. Xue, X. Wang and J. Wu, *Angew. Chem.*, 2024, **136**, e202404730.
30 Q. Fang, S. Ye, L. Zheng, H. Wang, L. Hu, W. Gu, L. Wang, L. Shi and C. Zhu, *ACS Catal.*, 2024, **14**, 9235–9243.
31 H.-R. Zhao, C.-Z. Yuan, C. Zhou, W. Zhao, L. Zhang, C.-H. Li, L. Xin, F. Wu, S. Ye, X. Zhang and Y. Chen, *J. Energy Chem.*, 2024, **94**, 458–465.
32 P. W. Menezes, A. Indra, O. Levy, K. Kailasam, V. Gutkin, J. Pfrommer and M. Driess, *Chem. Commun.*, 2015, **51**, 5005–5008.
33 T. Wang, L. Miao, S. Zheng, H. Qin, X. Cao, L. Yang and L. Jiao, *ACS Catal.*, 2023, **13**, 4091–4100.
34 M. Weber-Stockbauer, O. Y. Gutiérrez, R. Bermejo-Deval and J. A. Lercher, *Catal. Sci. Technol.*, 2019, **9**, 509–516.
35 Y. Liu, L. Bai, Q. Jia, P. Li, Y. Yan, N. Yuan and X. Hao, *Chin. Chem. Lett.*, 2023, **34**, 107855.
36 J. Li, C. Yin, S. Wang, B. Zhang and L. Feng, *Chem. Sci.*, 2024, **15**, 13659–13667.